JOURNAL OF GEOPHYSICAL RESEARCH, VOL. 100, NO. D7, PAGES 14,147–14,162, JULY 20, 1995

Estimate of diffusion parameters of aircraft exhaust plumes near the tropopause from nitric oxide and turbulence measurements

U. Schumann, P. Konopka, R. Baumann, R. Busen, T. Gerz, H. Schlager, P. Schulte, and H. Volkert

DLR Oberpfaffenhofen, Institut für Physik der Atmosphäre, Weßling, Germany

Abstract. Horizontal and vertical plume scales and respective diffusivities for dispersion of exhaust plumes from airliners at cruising altitudes are determined from nitric oxide (NO) and turbulence data measured with the DLR Falcon research aircraft flying through the plumes. Ten plumes of known source aircraft were encountered about 5 to 100 min after emission at about 9.4 to 11.3 km altitude near the tropopause in the North Atlantic flight corridor at 8°W on three days in October 1993. The ambient atmosphere was stably stratified with bulk Richardson numbers greater than 10. The measured NO peaks had half widths of 500 to 2000 m with maximum concentrations up to 2.4 parts per billion by volume (ppbv), clearly exceeding the background values between 0.13 and 0.5 ppbv. For analysis the measured plumes are approximated by an analytical Gaussian plume model which accounts for anisotropic diffusion in the stably stratified atmosphere and for shear. Two methods are given to obtain diffusivity parameters from either the individual plume data or the set of all plume measurements. Using estimates of the emitted mass of NO per unit length, the vertical plume width is found to be 140 m on average. This width is related to mixing in the initial trailing vortex pair of the aircraft. The range of the plume data suggests vertical diffusivity values between 0 and 0.6 $m^2 s^{-1}$. The turbulence data exhibit strong anisotropic air motions with practically zero turbulent dissipation and weak vertical velocity fluctuations. This implies very small vertical diffusivities. The horizontal diffusivity is estimated as between 5 and 20 $m^2 s^{-1}$ from the increase of horizontal plume scales with time. For constant diffusivities, shear dominates the lateral dispersion after a time of about 1 hour even for the cases with only a weak mean shear of 0.002 s^{-1}.

1. Introduction

Emissions from subsonic aircraft at cruising altitude may affect the ozone distribution and be of climatological relevance and have therefore become the subject of several research projects [*Schumann*, 1994]. Because of nonlinearity of air chemistry and physics the effects of the emissions depend on how quickly the emissions get mixed with the ambient air [*Danilin et al.*, 1992; *Miake-Lye et al.*, 1993; *Karol and Ozolin*, 1994]. Behind each aircraft a wake is formed which passes through the jet, vortex, and dispersion regimes [*Hoshizaki et al.*, 1975]. The dispersion regime begins when the organized motion of the trailing vortex pair breaks up into turbulent motions and ends when this turbulence has decayed. Thereafter, a so-called diffusion regime follows in which atmospheric motions control further dispersion. In the dispersion and diffusion regimes at timescales of minutes to several hours, the resultant plume of exhaust emissions spreads laterally from a few hectometers to a few kilometers mainly by atmospheric turbulence and shear in the ambient air. It can take time, of an order of a day, before all the plumes resulting from typical air traffic get homogeneously mixed within a flight corridor [*Schumann and Konopka*, 1994]. To compute the plume dispersion and the resultant chemical and physical effects on the atmosphere, one needs to know the effective diffusivities or equivalent dispersion model parameters.

Paper number 95JD01277.
0148-0227/95/95JD-01277$05.00

Subsonic jet aircraft usually cruise at altitudes near the tropopause [*Hoinka et al.*, 1993] where the atmosphere is usually stably stratified with large bulk Richardson numbers. Except near jet streams, frontal, and convective events, turbulence at those altitudes over ocean surfaces is often weak [*Fritts and Nastrom*, 1992]. Clear air turbulence may occur intermittently in regions of strong shear and breaking gravity waves [*Lilly et al.*, 1974; *Nastrom and Gage*, 1985; *Dewan*, 1985]. Turbulence may also originate from the aircraft or from processes in the plume itself, e.g., when contrails are being formed [*Knollenberg*, 1972]. Stable stratification counteracts vertical motions so that mixing is much slower in the vertical than in the horizontal directions. Stratification and shear cause anisotropic turbulent diffusion to a degree depending on the Richardson number [*Hunt*, 1985; *Kaltenbach et al.*, 1994; *Schumann and Gerz*, 1995]. Turbulent plume mixing is caused by motion scales smaller or comparable to the plume diameter [*Gelinas and Walton*, 1974]. Motions can be classified as turbulent only when the Ozmidov scale, also known as outer scale or buoyancy scale, is much larger than the Kolmogorov scale [*Stillinger et al.*, 1983; *Weinstock*, 1992]. For a strongly, stably stratified environment, the wakes tend to shrink vertically and stretch horizontally, part of the wake energy propagates away by gravity waves, and wakes show meandering motions [*Lilly*, 1983]. Hence the mixing of aircraft plumes follows classical turbulent

diffusion concepts only approximately. Nevertheless, practical plume models, as in the works of *Danilin et al.* [1992] and *Rodriguez et al.* [1994], usually rely on the existence of effective diffusivities and require corresponding data.

Observations are rare from which the effective diffusivities near the tropopause can be determined [*Lilly*, 1983; *Tank*, 1994]. Turbulent diffusion is usually estimated from either dissipation rates deduced from measured inertial-range spectra or structure functions or from vertical velocity variance [*Hunt*, 1985; *Schumann and Gerz*, 1995] measured with aircraft, balloon or radar systems [*Lilly et al.*, 1974; *Cadet*, 1977; *Barat*, 1982; *Woodman and Rastogi*, 1984]. A $-5/3$ power law of turbulence variances is often observed but may reflect other than inertial-range turbulence regimes [*Lilly*, 1983]. Turbulence intensities and dissipation rates vary intermittently in space and time and their mean values are strongly dependent on altitude, season, and the type of the underlying terrain. When nonzero, the measured dissipation values vary typically between 10^{-6} and 10^{-4} m^2 s^{-3}. The stratosphere over the North Atlantic shows relatively little turbulence on average [*Nastrom and Gage*, 1985; *Tank*, 1994]. Estimates of vertical diffusivities due to stratospheric turbulence over oceans vary from 0.012 to 0.3 m^2 s^{-1} [*Lilly et al.*, 1974]. Taking contrails in the upper troposphere as tracers for plumes, *Knollenberg* [1972] and *Joseph et al.* [1975] deduced effective horizontal diffusivities between 15 and 100 m^2 s^{-1}, respectively, but could not distinguish between broadening of the plumes by turbulence and by shear. *Knollenberg* [1972] reported a shear value of 0.012 s^{-1}, while that value is unknown in the case of Joseph's analysis of satellite data. The strong impact of mean [*Monin and Yaglom*, 1971; *Smith*, 1982] or fluctuating [*Young et al.*, 1982] shear on plume dispersion is well known, but corresponding data are missing for the tropopause region. Whereas shear might be computable from models, the small-scale shear fluctuations are usually unknown. In situ observations of various aircraft exhaust gases have been reported by *Arnold et al.* [1992] and *Fahey et al.* [1995]; but these studies did not investigate plume dispersion.

Recently, we obtained aircraft-borne nitric oxide (NO) measurements simultaneously with turbulence data during flights performed near the tropopause in the North Atlantic air traffic corridor in October 1993 [*Schlager et al.*, 1994]. The data clearly show encounters with exhaust plumes of several commercial jet airliners. In this paper the data are analyzed to determine the properties of the plumes and to learn about the mixing in the atmosphere under such conditions. For this purpose we approximate the mixing process by a Gaussian plume model with a constant but anisotropic diffusivity tensor and uniform vertical shear of the wind component perpendicular to the plume axis. An analytical solution is known for this process [*Konopka*, 1995] which generalizes special solutions, as given by *Novikov* [1958], *Monin and Yaglom* [1971], and *Smith* [1982]. It allows for arbitrary Gaussian initial plume shapes, anisotropic diffusion tensors, and shear. The theory also applies to time-dependent shear and diffusivities as well as to sedimenting and linearly, chemically reacting species, but these properties are not used in this paper.

The difficulty in analyzing the mixing properties of plumes from the few airborne measurements comes from the fact that only the horizontal concentration profiles in the plumes are measured directly. To determine the vertical scale of plumes, the source strength of the plume and the initial mixing in the wake of the emitting aircraft have to be estimated. Furthermore, the horizontal plume width depends on the plume distortion caused by shear, the values of which are strongly scale dependent.

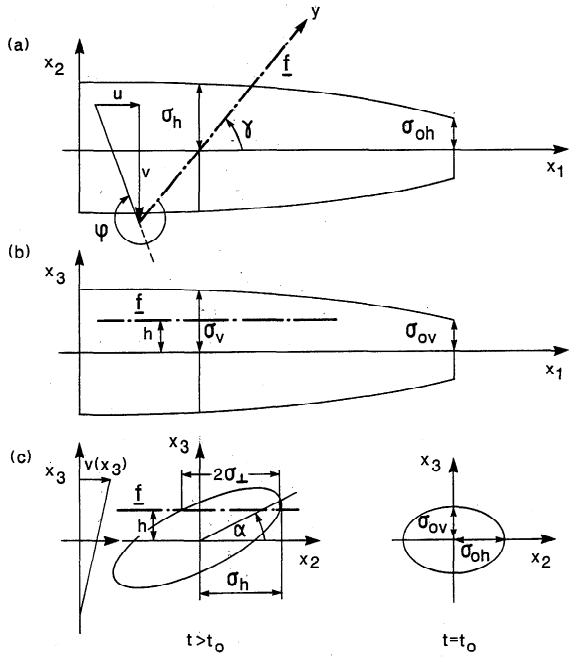

Figure 1. Sketch of an exhaust-emission plume of an aircraft flying along the x_1 axis in (a) the horizontal plane x_1-x_2, (b) in the vertical plane x_1-x_3, and (c) in the cross-section x_2-x_3; σ_{0h} and σ_{0v} are the horizontal and vertical standard deviations of the plume at $t = t_0$; σ_h and σ_v denote these values at $t > t_0$. Plume half widths are 2.2 times the corresponding standard deviations. Angle α denotes the plume tilt by vertical shear of the wind component v perpendicular to x_1 and by anisotropic turbulent diffusion. The track **f** of the measuring aircraft (Falcon) possesses the angle γ and altitude difference h relative to the x_1 axis; $\sigma_\perp$ refers to the projection of the measured plume width σ_f onto the x_2-x_3 plane; ϕ is the wind direction related to the flight track (which is in the northern direction).

The paper is organized as follows: Section 2 describes the Gaussian plume model, simplified as required for this study; section 3 explains the concept by which the diffusion coefficients are related to the measurements; and section 4 describes how the various model parameters are determined. The results are given in section 5. Section 6 compares the measured turbulence with models and climatologies. The conclusions are collected in section 7.

2. Gaussian Plume Model

We consider the concentration $\rho(x_1, x_2, x_3, t) = \rho(x_1, \mathbf{x}, t)$ above a uniform background level as caused by emissions from a particular aircraft flying along the x_1 coordinate as a function of time t. The vector $\mathbf{x} = (x_2, x_3)$ measures the coordinates within the plume's cross sections; x_3 is the vertical coordinate; see Figure 1. The total mass of the emitted species per unit length along the flight path is c (in kilograms per meter). We assume that the emitted species (we will consider NO for this purpose and assume a constant NO/NO$_x$ ratio for each plume) are chemically, sufficiently inert so that c = const. The initial mixing in the vortex regime is not modeled. Instead, we begin our considerations at the end of the vortex regime and assume that for $t = 0$, the concentration field in the plane

perpendicular to the flight path can be approximated by a Gaussian distribution

$$\rho(x_1, \mathbf{x}, 0) = c\varphi(\mathbf{x}, 0, \hat{\boldsymbol{\sigma}}_0). \tag{1}$$

Here φ denotes the Gaussian function, generally defined by

$$\varphi(\mathbf{x}, \bar{\mathbf{x}}, \hat{\boldsymbol{\sigma}}) := (2\pi)^{-n/2}(\det\hat{\boldsymbol{\sigma}})^{-1/2} \cdot \exp\left[-\tfrac{1}{2}(\mathbf{x} - \bar{\mathbf{x}}) \cdot \hat{\boldsymbol{\sigma}}^{-1} \cdot (\mathbf{x} - \bar{\mathbf{x}})\right], \tag{2}$$

where $\bar{\mathbf{x}}$ is a n-dimensional vector denoting the centroid of φ and $\hat{\boldsymbol{\sigma}}$ abbreviates the symmetric and positive-definite $n \times n$ variance matrix of φ. For the two-dimensional concentration field in the plume's cross section, $n = 2$. Furthermore, the initial plume variance matrix $\hat{\boldsymbol{\sigma}}_0$ is assumed to be diagonal,

$$\hat{\boldsymbol{\sigma}}_0 = \begin{pmatrix} \sigma_{0h}^2 & 0 \\ 0 & \sigma_{0v}^2 \end{pmatrix}. \tag{3}$$

Here σ_{0h} and σ_{0v} are given horizontal and vertical standard deviations of the initial plume concentration profile related to half widths by approximately $2.2\sigma_{0h}$ and $2.2\sigma_{0v}$, respectively. The centroid $\bar{\mathbf{x}}$ is assumed to be zero for this initial field.

During the plume dispersion we assume a time-independent horizontal wind which changes linearly with x_3. Mixing and shear distortion along the plume's axis are neglected because of the much smaller gradients in that direction. In the x_2-x_3-plane the plume gets advected and distorted by the horizontal mean wind component $v(x_3) = v_0 + sx_3$ perpendicular to the plume, where v_0 and s denote the mean value at flight level and the constant wind shear, respectively. Further, we consider turbulent diffusion with an assumed constant but anisotropic diffusivity tensor D_{ij}, with horizontal, vertical, and skewed components $D_h = D_{22}$, $D_v = D_{33}$, and $D_s = (D_{23} + D_{32})/2$. The diffusivity tensor is anisotropic and nonsymmetric because of anisotropic turbulence in sheared and stratified flows [*Kaltenbach et al.*, 1994]. To describe mixing, the diffusivity tensor has to be positive definite,

$$D_h, D_v > 0, \qquad D_s^2 < D_h D_v. \tag{4}$$

For a frame of reference moving with the mean flow velocity at the plume's axis the concentration field ρ for $t > 0$ satisfies the two-dimensional diffusion equation

$$[\partial_t + sx_3\partial_{x_2} - D_h\partial_{x_2}^2 - D_v\partial_{x_3}^2 - 2D_s\partial_{x_2}\partial_{x_3}]\rho(\mathbf{x}, t) = 0, \tag{5}$$

with the initial condition (1). According to *Konopka* [1995] the solution of (5) is

$$\rho(x_1, \mathbf{x}, t) = \rho(\mathbf{x}, t) = c\varphi(\mathbf{x}, 0, \hat{\boldsymbol{\sigma}}(t)), \tag{6}$$

with a positive-definite and symmetric variance matrix

$$\hat{\boldsymbol{\sigma}}(t) = \begin{pmatrix} \hat{\sigma}_h(t) & \hat{\sigma}_s(t) \\ \hat{\sigma}_s(t) & \hat{\sigma}_v(t) \end{pmatrix}, \tag{7}$$

$$\sigma_h^2(t) := \hat{\sigma}_h(t) = \tfrac{2}{3}s^2D_vt^3 + (2D_s + s\sigma_{0v}^2)st^2 + 2D_ht + \sigma_{0h}^2, \tag{8}$$

$$\hat{\sigma}_s(t) = sD_vt^2 + (2D_s + s\sigma_{0v}^2)t, \tag{9}$$

$$\sigma_v^2(t) := \hat{\sigma}_v(t) = 2D_vt + \sigma_{0v}^2. \tag{10}$$

The inverse matrix $\hat{\boldsymbol{\sigma}}^{-1}$, as required in (2), exists because $\hat{\boldsymbol{\sigma}}$ is a positive-definite matrix.

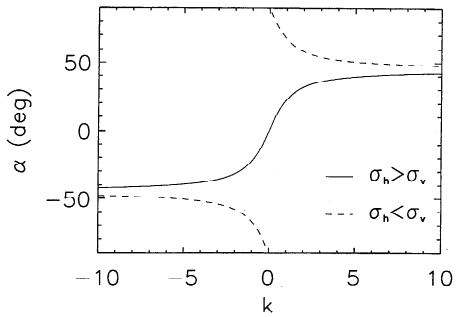

Figure 2. Plume tilt angle α versus parameter k; see equation (11).

The solution (6) satisfies the normalization condition

$$\int_{-\infty}^{\infty}\int_{-\infty}^{\infty} \rho(\mathbf{x}, t)\, dx_2\, dx_3 = c.$$

One-dimensional averages are

$$\int_{-\infty}^{\infty} \rho(\mathbf{x}, t)\, dx_2 = c\varphi(x_3, 0, \hat{\sigma}_v(t)),$$

$$\int_{-\infty}^{\infty} \rho(\mathbf{x}, t)\, dx_3 = c\varphi(x_2, 0, \hat{\sigma}_h(t)).$$

Consequently, σ_h and σ_v can be understood as horizontal and vertical standard deviations of the plume projections onto the horizontal and vertical planes, respectively.

The lines of constant density in the x_2-x_3 plane are ellipses, with the (larger) principal axis inclined by the tilt angle α relative to the horizontal with

$$\sin\alpha = \frac{k}{\sqrt{2}}[1 + k^2 \mp (1 + k^2)^{1/2}]^{-1/2}, \qquad k := \frac{2\hat{\sigma}_s}{|\hat{\sigma}_h - \hat{\sigma}_v|}, \tag{11}$$

where the signs $\mp$ correspond to $\sigma_h > \sigma_v$ and $\sigma_h < \sigma_v$, respectively. For $\sigma_h = \sigma_v$, the tilt angle α amounts to $\pi/4$. The possible values of α are shown in Figure 2. For $\hat{\sigma}_s \geq 0$ and $\sigma_h > \sigma_v$, one obtains $k \geq 0$ and $0 \leq \alpha \leq \pi/4$. The range $s \geq 0$ corresponds to $0 \leq \alpha \leq \pi/4$, and s and D_s are of the same sign.

The relations (8) to (10) can be simplified for certain time intervals. The cubic term dominates after a critical time t_{cubic},

$$t_{\text{cubic}} := \frac{3}{2D_v|s|}\left[D_s' + \left(D_s'^2 + \frac{4}{3}D_hD_v\right)^{1/2}\right], \qquad D_s' := |D_s| + \tfrac{1}{2}\sigma_{0v}^2|s|, \tag{12}$$

after which the dispersion depends mainly on the vertical diffusivity D_v, the wind shear s, and the initial standard deviations σ_{0v} and σ_{0h}, so that

$$\sigma_h^2(t) \approx \tfrac{2}{3}s^2D_vt^3 + \sigma_{0h}^2, \qquad \hat{\sigma}_s(t) \approx sD_vt^2, \qquad \sigma_v^2(t) = 2D_vt + \sigma_{0v}^2. \tag{13}$$

For $t \ll t_{\text{quadr}}$, with

$$t_{\text{quadr}} := \frac{\sigma_{0v}^2}{D_v} - \frac{2D_s}{sD_v}, \tag{14}$$

the following approximation can be used:

$$\sigma_h^2(t) \approx s^2\sigma_{0v}^2 t^2 + 2D_h t + \sigma_{0h}^2, \qquad \hat{\sigma}_s(t) \approx s\sigma_{0v}^2 t,$$
$$\sigma_v^2(t) = \sigma_{0v}^2 + 2D_v t. \tag{15}$$

In particular, $t \ll t_{\text{quadr}}$ is valid for $D_v \approx D_s \ll D_h$. In this case, shear dominates the horizontal dispersion after

$$t_{\text{shear}} := 2D_h/(\sigma_{0v}^2 s^2). \tag{16}$$

The vertical plume scale stays constant, $\sigma_v^2(t) \approx \sigma_{0v}^2$, if, in addition, $t \ll t_{\text{vert}}$, with

$$t_{\text{vert}} := \frac{\sigma_{0v}^2}{2D_v}. \tag{17}$$

3. Method for Determination of Diffusion Coefficients

The explicit solution (6) determines the spatial and temporal field of the concentration above background due to emission of an individual aircraft, provided that the initial parameters σ_{0h}, σ_{0v}, c and the model parameters s, D_h, D_v, and D_s are known. Here we are interested in the inverse problem, i.e., in determining the diffusion coefficients from observed concentration profiles.

For this purpose we now derive several relations from which the diffusion coefficients can be calculated in terms of measurable properties of the observed concentration peaks. To simulate the observed concentration data, we determine the cross section spanned by solution (6) and a straight line **f** representing the flight path of the measuring aircraft (see Figure 1),

$$\mathbf{f}(y) = \begin{pmatrix} y\cos\gamma \\ y\sin\gamma \\ h \end{pmatrix}, \tag{18}$$

where y is the space coordinate along the track of the measuring aircraft and γ denotes the angle and h the distance between the main axis of the plume given by the x_1 axis and the flight track. The measurable concentration ρ_f along line (18) follows from

$$\rho_f(y, t) := \rho(f_1(y), f_2(y), f_3(y), t). \tag{19}$$

Inserting (18) into (6), one obtains ρ_f as a one-dimensional Gaussian function (equation (2) with $n = 1$),

$$\rho_f(y, t) = A(t)\varphi(y, \bar{y}_f(t), \hat{\sigma}_f(t)), \tag{20}$$

with

$$A(t) := \frac{c}{\sin\gamma}\,\varphi(h, 0, \hat{\sigma}_v(t)), \tag{21}$$

$$\bar{y}_f(t) := \frac{h}{\sin\gamma}\frac{\hat{\sigma}_s(t)}{\hat{\sigma}_v(t)}, \tag{22}$$

$$\sigma_f^2(t) := \hat{\sigma}_f(t) := \frac{\hat{\sigma}_v(t)\hat{\sigma}_h(t) - \hat{\sigma}_s^2(t)}{\hat{\sigma}_v(t)\sin^2\gamma}. \tag{23}$$

Here A, $\bar{y}_f$, and σ_f denote the integrated concentration, the centroid, and the standard deviation of the concentration peak profile ρ_f, respectively. Note that A and $\bar{y}_f$ depend on h, while σ_f is independent of the vertical displacement. The standard deviation normal to the plume axis at the altitude of the flight track **f** is

$$\sigma_\perp := \sigma_f|\sin\gamma|. \tag{24}$$

We emphasize the difference between $\sigma_\perp$ and σ_h; in general, $\sigma_\perp \le \sigma_h$ (see Figure 1c). Because of the normalization property,

$$A(t) = \int_{-\infty}^{\infty} \rho_f(y, t)\, dy, \tag{25}$$

where A is the integral area under the function ρ_f. Hence the vertical plume variance $\hat{\sigma}_v$ can be estimated from (21) in terms of the measured area A, provided also c, γ, and h are known. On the other hand, (23) gives only an implicit relation between σ_f and the remaining plume variance components $\hat{\sigma}_h$ and $\hat{\sigma}_s$, which cannot be determined uniquely therefore.

To estimate the diffusion coefficients D_v, D_h, and D_s from the measured parameters, we start from (24), (23), and (8) to (10), giving $\sigma_\perp$ as a rational function of time,

$$\sigma_\perp^2(t) := \tfrac{2}{3}s^2D_v t^3 + (2D_s + s\sigma_{0v}^2)st^2 + 2D_h t + \sigma_{0h}^2 - (2D_v t + \sigma_{0v}^2)^{-1}[sD_v t^2 + (2D_s + s\sigma_{0v}^2)t]^2. \tag{26}$$

This expression can be approximated as a t polynomial,

$$\sigma_\perp^2(t) \approx \sigma_{0h}^2 + a_1 t + a_2 t^2 + a_3 t^3 + , \cdots, + . \tag{27}$$

A cubic approximation is sufficient for $t \ll t_{\text{vert}}$ and $t \gg t_{\text{vert}}$; see (17). In the first case for $t \ll t_{\text{vert}}$, the coefficients a_1, a_2, and a_3 are

$$a_1 = 2D_h, \qquad a_2 = -2sD_s\left(1 + \frac{2D_s}{s\sigma_{0v}^2}\right),$$
$$a_3 = -\tfrac{4}{3}s^2D_v\left(1 + \frac{3D_s}{s\sigma_{0v}^2}\right). \tag{28}$$

If also $t \ll t_{\text{lin}}$, with

$$t_{\text{lin}} := (2a_3)^{-1}[-a_2 - (a_2^2 - 4a_1a_3)^{1/2}], \tag{29}$$

then a linear approximation

$$\sigma_\perp^2(t) \approx \sigma_{0v}^2 + 2D_h t \tag{30}$$

holds. In the second case for $t \gg t_{\text{vert}}$, the coefficients are

$$a_1 = 2D_h - \frac{(s\sigma_{0v}^2 + 2D_s)^2}{2D_v}, \qquad a_2 = 0, \qquad a_3 = \tfrac{1}{6}s^2D_v. \tag{31}$$

On the basis of these relations the diffusion coefficients D_v, D_h, and D_s can be determined by the two following methods:

Method A

For given values of A, γ, c, and σ_{0v} we calculate σ_v from the implicit equation (21) by determining the roots of the function

$$f(x) := x - \exp\left(-\frac{r^2}{2x^2}\right) = 0, \tag{32}$$

with

$$x := \frac{\sigma_v}{a}, \qquad r := \frac{h}{a}, \qquad a := \frac{c}{\sqrt{2\pi A}\sin\gamma}.$$

There are two roots (in addition to $x = 0$) of (32), as plotted in Figure 3 for different values of r. For $r \to 0$ (i.e., $h \to 0$), only the solution $x = 1$ (i.e., $\sigma_v = a$) is valid. Therefore the lower branch of the two solutions $x(r)$ (dotted curve in Figure 3) has to be ignored. Because of

$$r_{\max} = x_{\min} = \frac{1}{\sqrt{e}} \approx 0.61, \tag{33}$$

both the distance h and the standard deviation σ_v, for given values of c, A, and γ, have to stay in the limits

$$0 \le h \le h_{\max} := \frac{a}{\sqrt{e}}, \tag{34}$$

$$\sigma_v^{\min} := \frac{a}{\sqrt{e}} \le \sigma_v \le \sigma_v^{\max} := a. \tag{35}$$

Hence even when h is unknown, lower and upper bounds for h are given from which one obtains bounds $\sigma_v^{\min}$ and $\sigma_v^{\max}$ which embrace the best estimate mean value σ_v with 20% uncertainty. Note that $\sigma_v^{\min} = h_{\max}$. If the analysis is repeated for the same or for similar plumes at various times, a fit of (10) to the data determines the vertical diffusivity D_v. The remaining diffusion coefficients D_h and D_s cannot be determined by this method.

Method B

Here the starting point of our discussion is the cubic approximation (27) which is valid for $t \ll t_{\text{vert}}$ and for $t \gg t_{\text{vert}}$. The method requires that measured values $\sigma_\perp$ are available at various ages of one or a set of similar plumes within the proper time period. Furthermore, we have to assume that the wind shear s stays about constant during this period. Then, these data form the base to fit polynomial (27) giving best estimate values for the coefficients a_1, a_2, and a_3. Once these coefficients are known, some or all of the requested diffusivity parameters can be estimated depending on when the measurements are made. In principle, all diffusivity components can be determined if $t \ll t_{\text{vert}}$. In this case, the coefficients D_v, D_h, and D_s can be expressed in terms of the parameters a_1, a_2, and a_3 from (28) and can all be evaluated, provided the shear value s and the initial plume variances σ_{0v}^2 and σ_{0h}^2 are known. If, however, $t \ll t_{\text{lin}}$, only the horizontal diffusivity D_h can be determined from (30). In the other time range, $t \gg t_{\text{vert}}$, one obtains the vertical diffusivity D_v from the cubic coefficient a_3, (see (31)), but the remaining diffusion coefficients cannot be determined uniquely since $a_2 = 0$ and a_1 is a function of both D_h and D_s. Note that method B is independent of c and h as long as the measured concentration increase is large enough to discriminate the peaks from the background level.

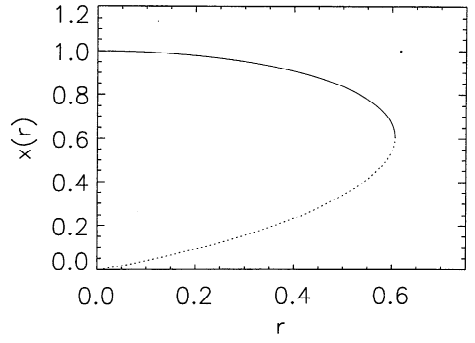

Figure 3. Solutions of equation (32) for different values of the parameter r. Only the top branch of the curve (solid) is physically valid.

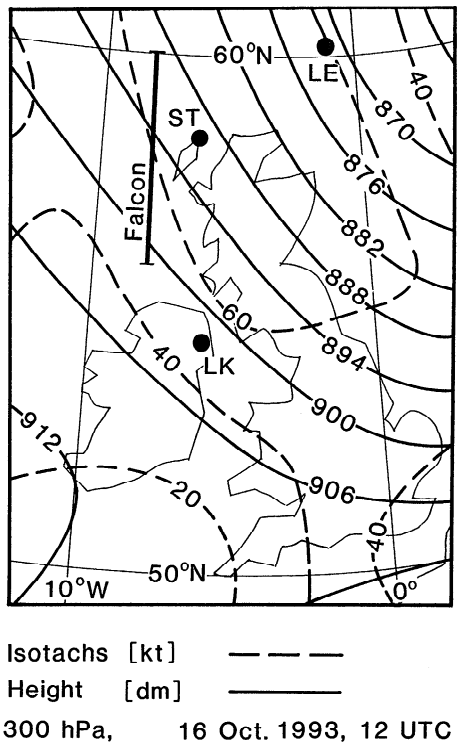

Figure 4. Flight track of the Falcon along 8°W, west of Scotland in a weather map for 300 hPa of 1200 UTC, October 16, 1993, adopted from routine analysis of U.K. Meteorological Office. Geopotential heights in dam (solid curves), isotachs in knots (dashed curves), 1 knot $\approx$ 0.5 m s^{-1}. Symbols denote the stations LK, Long Kesh, ST, Stornoway, and LE, Lerwick.

4. Evaluation of Experimental Data

The analysis methods described above are applied to data measured on October 16, 17, and 20, 1993, on board the Falcon research aircraft of the DLR (Deutsche Forschungsanstalt für Luft- und Raumfahrt, the German air and space research establishment) equipped with a fast response NO chemiluminescence detector and a turbulence-measuring system together with other scientific instruments. Several NO peaks were detected which can be related to exhaust plumes of individual source aircraft. The Falcon crossed the North Atlantic air traffic corridor west of the Scottish coastline along 8°W (see Figure 4) covering the latitudes between about 56° and 60°N, at four different flight levels of 310, 330, 350, and 370 hft (hectofeet) corresponding to pressure levels of 287, 261, 238, and 216 hPa and nominal altitudes of 9.4, 10.1, 10.7, and 11.3 km, respectively. Along each flight leg the flight level of the Falcon was kept constant to about ±5 m.

The meteorological situation in the upper troposphere near the flight tracks was similar for all three observation periods. Between October 16 and 20, 1993, the circumpolar flow at the 200-hPa level was characterized by three wide quasi-stationary

Table 1. Tropopause Observations at 1200 UTC at Stations LK, Long Kesh (6°06′W, 54°29′N), ST, Stornoway (6°19′W, 58°13′N), and LE, Lerwick (1°11′W, 60°08′N)

Station	p_{tp}, hPa	h_{tp}, km	T_{tp}, K	v_{tp}, m s^{-1}	ϕ, deg	$\lvert\nabla_h v\rvert$, 10^{-5} s^{-1}
			October 16			
LK	203	11.7	212	21	315	
ST	231	10.8	214	31	320	3.5
LE	379	7.60	223	24	340	
			October 17			
LK	210	11.5	210	11	310	
ST	227	11.0	208	20	315	4.9
LE	259	10.1	213	20	310	
			October 20			
LK	225	11.0	213	43	340	
ST	235	10.8	216	50	335	5.6
LE	280	9.60	216	29	255	

Here p_{tp}, h_{tp}, and T_{tp} are the pressure, the standard atmosphere altitude, and the temperature of the tropopause, respectively. The horizontal wind speed and its direction are denoted by v_{tp} and ϕ. Furthermore, $\lvert\nabla_h v\rvert$ is the horizontal gradient of wind speed at synoptic scales of 300 hPa.

troughs separated by ridges. All our measurements were obtained at the rearward side of the European trough (trough line roughly from Norway to France) with northwesterly winds between 20 and 50 m s^{-1} and just ahead of a well-developed ridge over the Atlantic. Tropopause heights, temperatures, and winds are given in Table 1 for radio stations Long Kesh and Stornoway in the vicinity of the flight tracks and for Lerwick farther to the east (see Figure 4). The tropopause was always lower over Lerwick than at the two other stations because of the ridge-trough pattern. The horizontal wind speed at the tropopause was moderate, the tropopause temperature varied between 210 and 216 K, and the horizontal wind gradient at 300 hPa inferred from a synoptic analysis was relatively weak.

Figure 5 shows the wind and temperature profiles measured during the ascents and descents of the Falcon before or after flying along the flight legs. We see strong vertical variations with many thin sheets of different stability and shear. Similar temperature sheets have been found in the stratosphere by *Dalaudier et al.* [1994]. The various Falcon profiles differ due to spatial and temporal variations of the meteorological fields. Any model of plume dispersion has to be based on suitable mean values of these profiles. Therefore we use the linear fits as indicated between neighboring flight levels to characterize mean stratification and shear. Table 2 lists the corresponding values for the Brunt-Väisälä frequency N, the vertical gradient of the horizontal wind direction, the vertical shear of total wind

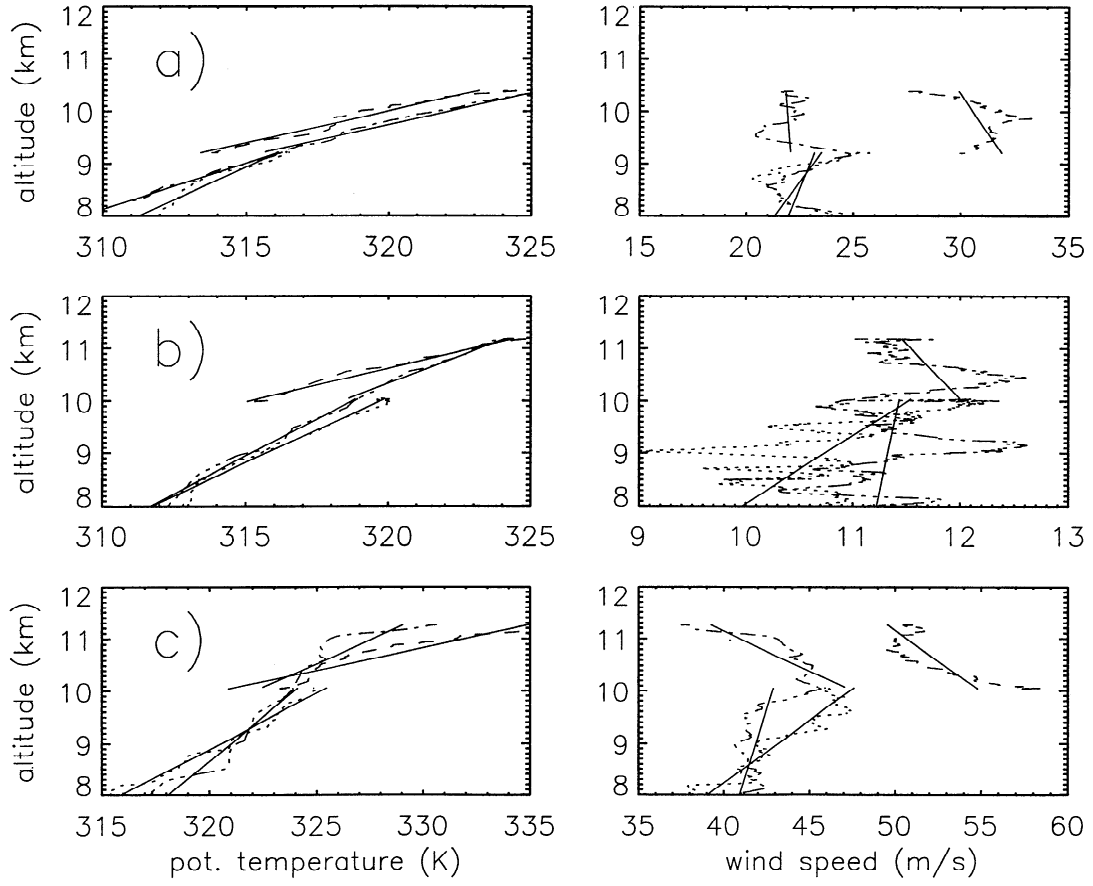

Figure 5. Potential temperature and wind speed versus altitude, measured in (a) October 16, (b) 17, and (c) 20, during ascents and descents of the Falcon. The dotted, dashed, dashed-dotted, and dashed with triple-dot curves denote the profiles obtained during the first ascent (≈56°N), second ascent (≈60°N), and first and second part of the descent (≈56°N), respectively. Linear approximations to the profiles (solid curves) were calculated over scales of about 1 km.

Table 2. Data of Falcon Flights Together With Meteorological Parameters

FL hft	N 10^{-2} s^{-1}	$\lvert\nabla_v\phi\rvert$, deg km^{-1}	S, 10^{-3} s^{-1}	Ri	Δz, km	NO, pptv
			October 16			
310	1.7 ± 0.2	4 ± 2	2 ± 2	72	−1.4	130–250
350	1.9 ± 0.1	4 ± 2	2 ± 2	90	−0.3	150–280
			October 17			
330	1.4 ± 0.3	1 ± 1	1 ± 1	200	−1.4	150–220
370	1.7 ± 0.2	3 ± 1	1 ± 1	290	±0.3	200–500
			October 20			
370	1.9 ± 0.4	10 ± 2	6 ± 2	10	0.3	380–500

FL, flight level; N, Brunt Väisälä frequency; $\lvert\nabla_v\phi\rvert$, vertical gradient of the horizontal wind direction; S, (total) wind shear; Ri, bulk Richardson number; Δz, altitude difference between flight level and tropopause. Also listed is the range of mean background NO mixing ratios when averaged over about 100-km sections along the flight legs.

speed S, and the corresponding (bulk) Richardson number $Ri = N^2/S^2$, for the different flight levels and for all three days. The wind direction ϕ varied only very little with altitude and time. For vertically constant wind direction the effective shear perpendicular to the plumes could be computed for given ϕ and given angle γ of the flight tracks with respect to the northern direction from $s = S \sin(\phi - \gamma)$ but, obviously, with large uncertainties. However, as we will see, the shear or stratification data are not needed for diffusion analysis, except for estimating critical time limits. On the basis of the synoptic observations and the temperature soundings of the Falcon, most flight legs were in the upper troposphere (see Table 2) except for flights at FL 370 which exceeded the tropopause by about 300 m, at least in the northern parts.

The NO measurements were made with a chemiluminescence analyzer similar to that described by *Drummond et al.* [1985] with a detection limit of approximately 30 and 5 parts per trillion by volume (pptv) for an integration time of 1 s and 1 min, respectively. The instrument measures in cycles of 5-s period, consisting of two consecutive measurement modes with 1-s integration time, respectively, a zero-signal measuring mode of 1-s duration, and a total of 2 s for flushing of the reaction chamber between measuring and zero mode. The accuracy of the measurement depends mainly on calibration and count statistics. The calibration is performed by using a standard gas mixture and a dynamical dilution system with an uncertainty of about 5%. The statistical error depends on the number of photon counts detected during the integration period. For volume mixing ratios higher than 0.5 ppbv, the errors are smaller than 10% for 1-s integration time.

The observed NO volume mixing ratios for each flight leg measured with 1-s integration times are shown in Figure 6. The background values, when averaged over 100-km flight leg sections, vary between 130 and 500 pptv considering all flights (see Table 2) with variances of typically 50 pptv within each section. Generally, the mean values increase with altitude relative to the tropopause. Several NO peaks can be seen reaching between 0.6 and 2.4 ppbv. The 10 peaks with maxima exceeding the background mixing ratios by more than 0.4 ppbv, clearly above the variance of these values, are listed in Table 3. The NO signals for these peaks are plotted at a higher resolution in Figure 7. Most peaks include only 2 to 4 NO data points. Two peaks (numbers 1 and 10) are wider and show some asymmetry but a clear maximum. Hence a Gaussian fit can only give an approximation for the peak area and width. Contrails were visible for three of the ten plume events (numbers 2, 4, and 5). Similar peaks were found in simultaneous condensation nuclei measurements of *Hagen et al.* [1994]. The peak data are processed to estimate the diffusion coefficients in the following four steps.

Identification of the Source Aircraft

The call signs and the geographical positions versus time of all relevant airplanes passing the measuring area of the Falcon were documented by video records taken from the air traffic control radar display in Prestwick. Most airplanes flew in the so-called Shanwick airspace (Shannon and Prestwick radio-controlled airspace) and all flights were registered by the Civil Aviation Authority in London. The measured peaks are traced back to individual airliners by matching the time of peak measurements with the time when an airliner plume, as observed by radar and advected with the mean-wind (based on Falcon data), crossed the Falcon track. For the oldest plume the time difference reaches 80 s, which is small enough to identify the source aircraft without doubts. For each plume the geographical position, the time of measurement t_m, the age t (corrected for displacement with the wind), and the angle γ between the plume axis and the Falcon track are listed in Table 3. On the basis of the call signs and the date of the day of the flight it was possible to identify the various aircraft and engine types (see Table 4).

Peak Parameters

After subtraction of the measured background levels in the peak environment and transformation of time into space coordinates according to the airspeed of the Falcon ($v_F \approx 185$ m s^{-1}), the data were used to determine the quantities A and σ_f by means of a Gaussian fit (see Figure 7) with an accuracy of about 20%, and $\sigma_\perp$ is calculated from σ_f and γ according to (24). The results are listed in Table 3.

Source Intensity

For method A we need the source intensity. The source c of NO depends on the source of NO_x and the relative fraction of NO with respect to the NO_x abundances. *Arnold et al.* [1992] and *Fahey et al.* [1995] found that only a small fraction of NO_x is converted to other odd nitrogen species such as nitric acid. The model study of *Karol and Ozolin* [1994] suggests that in the case of intensive ambient air entrainment into the plume the NO_x oxidation may not be fully negligible during the first hours. Here we assume NO_x to be a conservative tracer.

To estimate the NO/NO_x concentration ratio without having measured NO_2 values, we assume that a photochemical equilibrium between NO and NO_2 is reached in the plumes with ages larger than 4 min. For known background ozone number density $n[O_3]$ (per cubic centimeters) the equilibrium ratio of the NO and NO_x number densities is

$$\frac{n[\mathrm{NO}]}{n[\mathrm{NO}_x]} = \frac{k_2}{k_1 n[\mathrm{O}_3] + k_2}, \tag{36}$$

where k_1 and k_2 denote the rate coefficient for the conversion of NO to NO_2 by the reaction with ozone and for the inverse conversion due to photolysis, respectively. The rate coefficient

$$k_1 = c_1 \exp\left(-\frac{T_1}{T}\right), \quad T_1 = 1370 \text{ K}, \quad c_1 = 2 \times 10^{-12} \text{ cm}^3 \text{ s}^{-1}$$

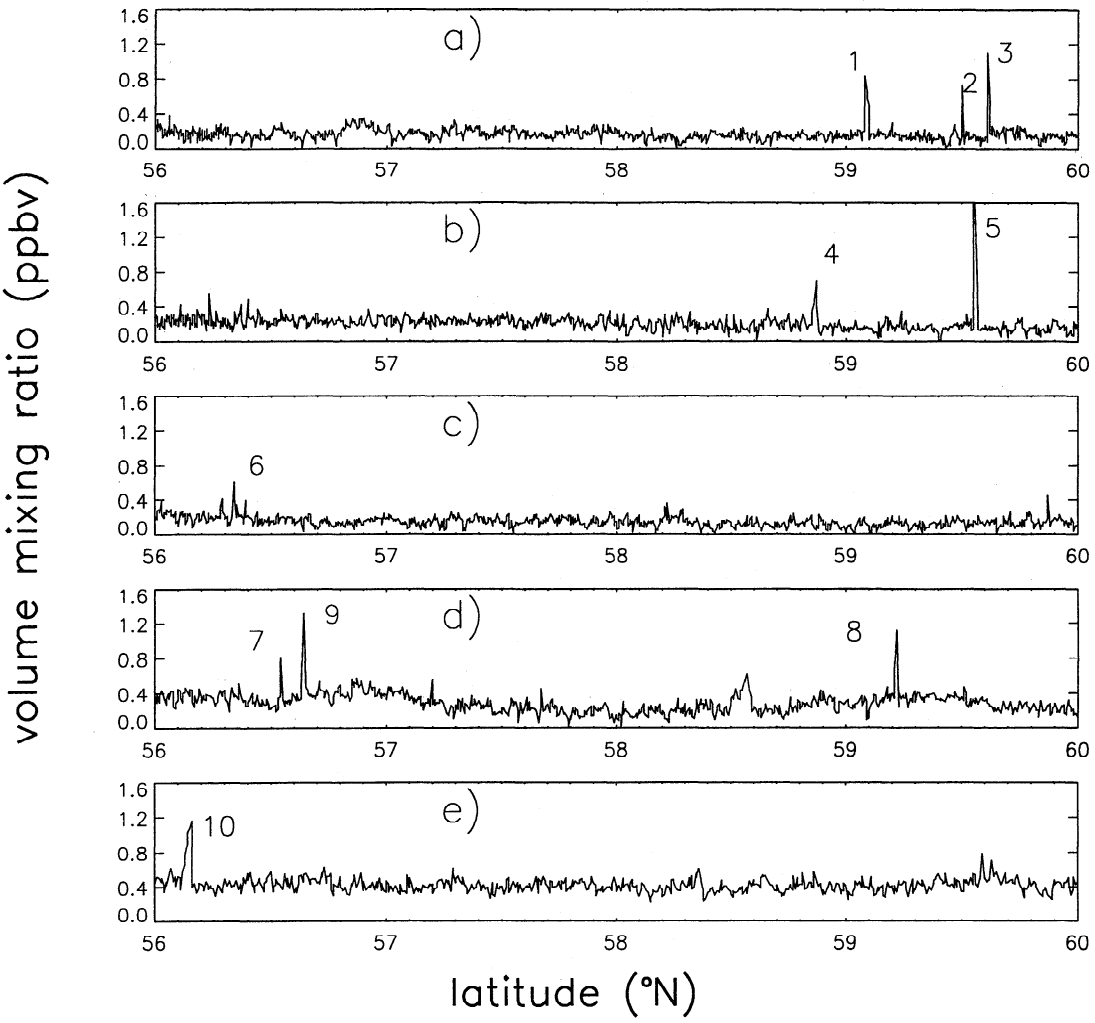

Figure 6. Measured NO volume mixing ratio versus latitude at different flight levels (in hectofoot) and dates: (a) FL = 350, October 16; (b) FL = 310, October 16; (c) FL = 330, October 17; (d) FL = 370, October 17; and (e) FL = 370, October 20. Peaks are numbered from 1 to 10 as in Table 3.

Table 3. Parameters of NO Peaks

Number	alt, km	lat, °N	T, K	t_m (UTC) h min^{-1} s^{-1}	t (age), min	A, ppbv m	σ_f, m	γ deg	$\sigma_\perp$, m
1	9.4	59.09	218	1443:21	61	1305	766	117	684
2	9.4	59.50	218	1447:54	45	388	258	134	186
3	9.4	59.61	218	1449:10	7.3	836	340	132	254
4	10.6	59.54	215	1516:04	95	827	569	127	456
5	10.6	58.86	214	1522:33	17	2033	370	131	280
6	10.0	56.34	217	0826:17	78	551	478	106	460
7	11.2	56.54	209	0941:44	71	630	433	109	410
8	11.2	59.20	210	0916:26	25	592	310	112	288
9	11.2	56.63	209	0940:47	4.5	828	344	109	326
10	11.2	56.13	214	1006:57	14	1645	912	112	847

Alt, altitude; lat, latitude; T, air temperature; t_m, UTC time at which Falcon crossed the plume; t, age of the plume; A, peak area of the measured NO volume mixing ratio; σ_f, standard deviation of the plume; γ, angle between the plume axis and the Falcon track; $\sigma_\perp$, horizontal standard deviation of the plume (perpendicular to the plume axis). All flights were performed along 8°W. Plumes 1–5, 6–9, and 10 were obtained October 16, 17, and 20, respectively.

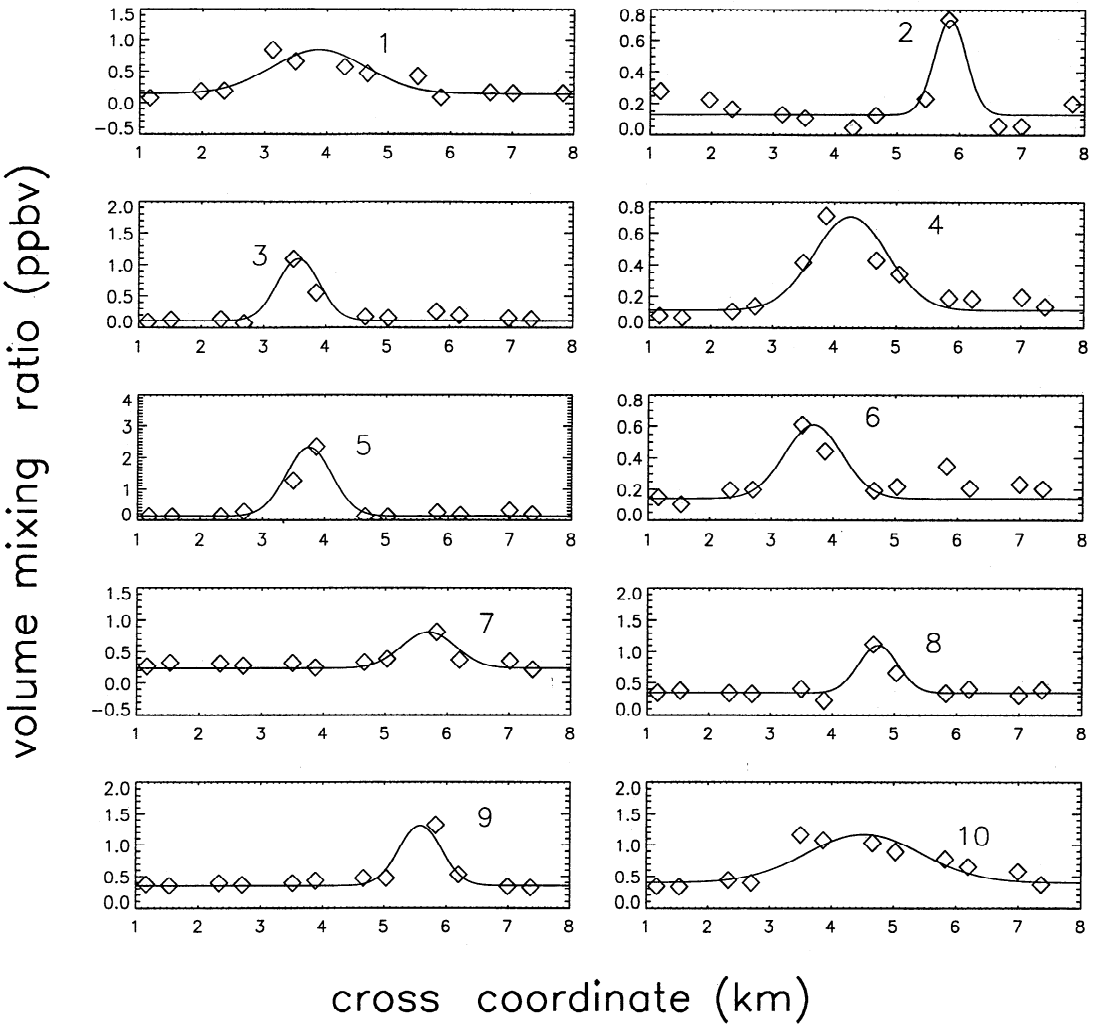

Figure 7. Peak NO volume mixing ratios versus flight distance of the Falcon with peak numbers as in Figure 6 and Table 3. Measured data, squares; Gaussian approximations, curves.

is taken, as in the work of *Brühl and Crutzen* [1988], as a function of the measured air temperature T (in degrees Kelvin). The photolysis rate coefficient k_2 depends on altitude and zenith angle and is calculated for each peak as in the work of *Ruggaber et al.* [1994]. The ozone number density is taken from the nearest ozonesonde at Lerwick on October 13 and 20, 1993, which reported ozone partial pressures of about 3 ± 0.5 mPa in the troposphere below 7 km altitude, and about 6.5 ± 1 mPa in the stratosphere above 9 km, with a gradual transition in between. The ozone concentrations used are interpolated

Table 4. Data of Aircraft

Number	Type	Engine	D	V, m s^{-1}	B, m	$W_{\pm}$, 10^6 N	w_s, m s^{-1}	σ_{0v}, m
1	B747	GE CF6-50E2	W	247	59.6	3.56/2.34	2.28	61.2
2	B767	RB 211-524H	W	235	47.6	2.00/1.65	2.11	56.6
3	B747	PW JT9D	W	247	59.6	3.56/2.34	2.28	61.2
4	B727	PW JT8D-7B	W	225	32.9	0.75/0.55	2.06	49.2
5	B747	PW JT9D	W	247	59.6	3.56/2.34	2.70	64.7
6	L1011	RR RB211-524B4	E	238	47.3	2.15/1.47	1.70	55.0
7	L1011	RR RB211-524B4	E	238	47.3	2.15/1.47	1.98	52.9
8	B747	GE CF6-50E2	E	247	59.6	3.56/2.34	1.92	51.3
9	B747-F	GE CF6-50E2	E	247	59.6	3.56/2.34	1.91	51.1
10	B747	PW JT9D-7J	E	247	59.6	3.56/2.34	1.95	38.6

Type, aircraft type; engine, engine type; D, flight direction (E, eastbound; W, westbound); V, aircraft speed; B, span width; $W_{\pm}$, weight of the aircraft (maximum takeoff weight/maximum no-fuel weight); w_s, induced downward velocity of the vortex pair; σ_{0v}, initial vertical standard deviation from equation (38) with $h_s = 2.2\sigma_{0v}$.

Table 5. Data Used to Determine Vertical Standard Deviations σ_v^{min} and σ_v^{max}

Number	c_f, kg km^{-1}	EI[NO_x], 10^{-3}	k_2, 10^{-2} s^{-1}	$n[O_3]$, 10^{12} cm^{-3}	NO/NO_x	dc[NO], 10^5 ppbv m^2	σ_v^{max}, m	σ_v^{max}, m
1	13.6	13.3	0.49	1.5	0.47	1.16	24.1	39.8
2	5.7	18.1	0.46	1.5	0.45	0.64	55.5	91.5
3	13.2	18.4	0.45	1.5	0.45	1.49	58.1	95.8
4	4.5	7.70	0.37	2.1	0.34	0.19	7.0	11.7
5	13.3	19.9	0.33	2.1	0.32	1.37	21.7	35.7
6	8.4	19.5	0.71	1.5	0.56	1.39	63.2	104
7	8.5	19.6	0.89	2.2	0.59	1.70	68.8	113
8	14.0	14.8	0.81	2.2	0.55	2.01	88.4	146
9	14.0	14.8	0.89	2.2	0.58	2.12	65.3	108
10	12.8	20.3	0.90	2.2	0.55	2.57	40.7	67.1

Here c_f, fuel consumption; EI[NO_x], emission index of NO_x; k_2, NO_2 photolysis rate coefficient; $n[O_3]$, ozone number density; NO/NO_x, concentration ratio determined from (36); dc[NO], source intensity of NO obtained from (37) with the dimension factor $d = M_{air}/(M_{NO}\rho_{air})$; σ_v^{min}, σ_v^{max}, minimal and maximal values of the vertical standard deviation calculated from (35), respectively.

ozonesonde data for the same altitude relative to the tropopause level. As a result, we obtain concentration ratios of NO and NO_x between 0.3 and 0.6 (see Table 5) with an estimated uncertainty of about 10%. (For future measurements the Falcon has now been equipped with NO_2 and ozone sensors, making the above considerations obsolete.)

The source intensity of NO_x depends on the fuel consumption c_f of the individual aircraft and on the emission index (EI) of NO_x, which depend, in turn, on the type of the aircraft, the type of engine, and the actual power setting of the engines. The cruising speeds, the fuel consumptions, and the EI of NO_x for each of the aircraft/engine combination, as listed in Table 4, have been kindly computed by F. Deidewig with methods described by *Deidewig* [1992] and *Deidewig and Lecht* [1994]. Consequently, the source intensity c of NO amounts to

$$c := c[\mathrm{NO}] = \frac{n[\mathrm{NO}]}{n[\mathrm{NO}_x]} \frac{M_{\mathrm{NO}} c_f \mathrm{EI}[\mathrm{NO}_x]}{M_{\mathrm{NO}_2}}, \qquad (37)$$

where M_{NO} and M_{NO_2} are the respective molar masses of the gases. The resultant source values c, with an estimated uncertainty of about 20%, are listed in Table 5. The table lists dc with $d = M_{air}/(M_{NO}\rho_{air})$ since the measurements are in terms of mixing ratios.

Initial Conditions at the Beginning of the Dispersion Regime

The Gaussian plume model is applied only in the dispersion and diffusion regimes, for plume ages larger than t_0. From now on, the time t of section 2 is replaced by $t_{eff} := t - t_0$. We need to estimate t_0 and the related initial vertical and horizontal standard deviations σ_{0v} and σ_{0h}. According to *Hoshizaki et al.* [1975] the dispersion regime follows the vortex regime after a time of about 100 s. In the early vortex regime, vertical motions dominate because of the downwind caused by the weight of the aircraft. After a time of the order of N^{-1} the downward motion gets limited by stratification and the plume spreads horizontally. From such general considerations, we assume, with unknown precision, $t_0 = 100$ s and $\sigma_{0h} \approx 250$ m. (We will see that this gives reasonable fits for the measured horizontal standard deviations of the young plumes.)

To determine σ_{0v}, we suppose that the vertical size of an aircraft exhaust plume is determined by the maximum vertical displacement of the trailing vortex pair at a given stratification, $h_s = w_s/N$, where w_s is the initial downward velocity of the vortex pair. Its impulse balances the weight W of the cruising aircraft and equals the lift produced at its wings. For elliptically loaded wings the Kutta-Joukowski law gives $W = (\pi/4)\rho_{air}BV\Gamma$ [*Donaldson and Bilanin*, 1975], where ρ_{air} is the density of air and B, V, and Γ are span width, speed, and mean circulation of the aircraft. For potential flow around the wing the circulation is conserved by the wingtip vortices which develop behind the aircraft, and the initial downward speed of the vortex pair is $w_s = \Gamma/(2\pi D)$, where $D = \pi B/4$ is the distance between the two vortices. In agreement with *Hoshizaki et al.* [1975] this results in

$$h_s = \frac{w_s}{N} = \frac{8W}{\pi^3 \rho_{air} N B^2 V}, \qquad (38)$$

as verified on the basis of vortex observations by *Schumann* [1994]. The required aircraft data are taken from *Jane* [1976] and the Brunt-Väisälä frequency N from Table 2. Since we do not know the actual weight of the aircraft at the time of plume encounter, we estimate W from either the maximum takeoff weight W_+ or the maximum no-fuel weight W_- depending on flight direction, assuming full tanks for westward and nearly empty tanks for eastward flying aircraft, respectively. Finally, σ_{0v} is related to h_s as if it would be the vertical half width of the plume at the beginning of the dispersion regime, $h_s \approx 2.2\sigma_{0v}$. Table 4 lists the aircraft data and the results for w_s and σ_{0v}. The values vary little (by about ±20%) among various aircraft, so that details of the aircraft are not very important for this analysis.

5. Plume Scales and Diffusivity Results

The given methods are now used to derive estimates for the diffusivities D_v, D_h, and D_s. First, we apply method A. Since the value of h is unknown, we compute maximum and minimum values σ_v^{max} and σ_v^{min} from (35) for $0 < h < h_{max}$, as given in (34). For uncertainties in c and A of about 20% we obtain σ_v^{max} and σ_v^{min} with an error of about 40%, respectively. The mean values of the upper and lower bounds amount to 49 and 81 m, giving an average plume half width of about 140 m, with no obvious dependence on time. The results are listed in Table 5. The calculated values of σ_v versus $t_{eff} := t - t_0$ are shown in the top panel of Figure 8. The errors of t amount to ≈5%. The squares mark the values of σ_{0v} (see Table 4). With the exception of peak 4, obtained for the oldest plume and the

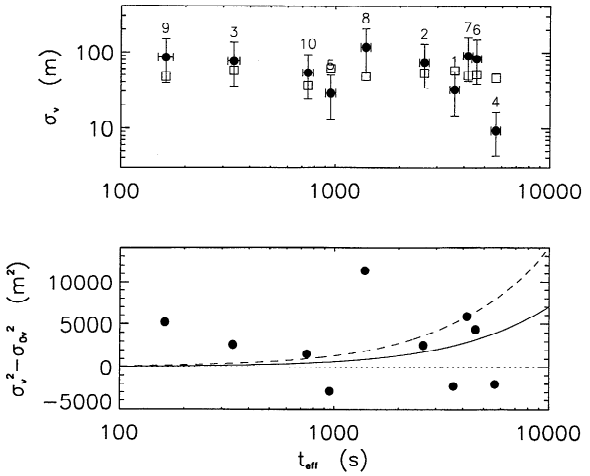

Figure 8. (top) Vertical standard deviations σ_v evaluated from the NO signals versus effective age $t_{\text{eff}} := t - t_0$ (circles with error bars) and the initial standard deviations σ_{0v} (squares) estimated from (38). Peak numbers are identified. (bottom) $\sigma_v^2 - \sigma_{0v}^2$ as evaluated (circles) and as predicted by the linear approximation (10) for $D_v = 0.3$ m^2 s^{-1} (solid curve), for $D_v = 0$ (dotted) and for $D_v = 0.6$ m^2 s^{-1} (dashed), versus effective plume age.

smallest aircraft, we see that the estimated initial plume scale due to vortex mixing stays within the error bounds of the deduced vertical plume scales. In the bottom panel of Figure 8 the differences $\sigma_v^2 - \sigma_{0v}^2$ are shown. These data scatter around zero with little mean trend. If one fits these data with the linear function (10), one obtains $D_v = 0.3$ m^2 s^{-1}, but values between 0 and 0.6 m^2 s^{-1} are equally consistent with the data.

Method B contains various alternatives depending on the critical times t_{vert} and t_{lin} (see (17) and (29)). For $\sigma_{0v} \approx 50$ m and $D_v \approx 0.3$ m^2 s^{-1}, $t_{\text{vert}} \approx 1$ hour. For $D_h < 20$ m^2 s^{-1} and $D_s \approx (D_v D_h)^{1/2}$, t_{lin} could be computed if the shear value s would be known. The various critical times and the measured ages t_{eff} of the plumes are plotted versus shear magnitude in Figure 9. For $|s|$ of the order of 0.002 s^{-1}, $t_{\text{cubic}} \approx 6$ hours, $t_{\text{shear}} \approx 50$ min, and $t_{\text{lin}} \approx 30$ min. Although we do not know the exact values of s for all peaks, we may assume that $|s| < |S|$ and $|S|$ is of the order of 0.002 s^{-1} for most cases except for

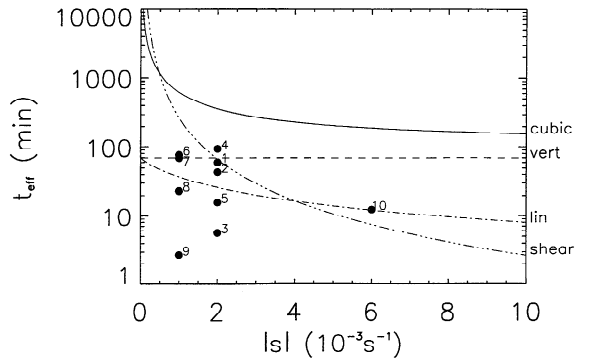

Figure 9. Critical times t_{cubic} (solid curve), t_{vert} (dashed), t_{lin} (dashed-dotted), and t_{shear} (dashed and triple dotted) for $D_v = 0.3$ m^2 s^{-1}, $D_h = 20$ m^2 s^{-1}, $|D_s| = 2.44$ m^2 s^{-1}, and $\sigma_{0v} = 50$ m, versus velocity shear magnitude $|s|$. Circles with numbers indicate ages and shear values of the respective measured plumes.

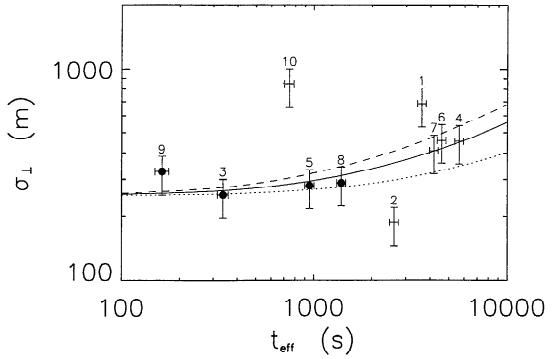

Figure 10. Values of $\sigma_\perp$ as measured for each peak versus effective age $t_{\text{eff}} := t - t_0$, numbered crosses with error bars. The circles identify cases which are fitted by the linear approximation (30) with $D_h = 12$ m^2 s^{-1}. Dotted and dashed curves depict the same approximations for $D_h = 5$ and $D_h = 20$ m^2 s^{-1}, respectively.

peak 10. Hence the relation $t_{\text{cff}} < t_{\text{lin}}$ is satisfied with sufficient reliability for peaks 3, 5, 8, and 9. Consequently, the linear approximation (30) can be used for these peaks. (Incidentally, these peaks all originate from comparable aircraft types B747 and B747-F.) Figure 10 shows the measured values of $\sigma_\perp$ versus t_{eff}. The data show large scatter and generally grow with time. At small times the data are close to the postulated initial value $\sigma_{0h} \approx 250$ m. The four events with ages satisfying the criterion for the linear approximation are indicated by circles. A least squares fit to these data gives $D_h \approx 12$ m^2 s^{-1} for the horizontal diffusivity, but values between 5 and 20 m^2 s^{-1} are also consistent with the data. We note that these results do not depend on the precise value of the shear magnitude. Although the scatter is large, most data (except for peaks 1, 2, and 10) fit the curve for $D_h = 12$ m^2 s^{-1} within the error bounds. Larger horizontal plume widths are found for peaks 1 and 10, perhaps because of stronger local shear or turbulence. In fact, peak 10 corresponds to the case with strongest shear and strongest velocity fluctuations (see below). We cannot rule out that part of this peak originates from an older plume. Also, the meandering of plumes, the spread due to stable stratification, and changes in the plume tilt angle α due to some horizontally varying vertical motions may explain strong variations in the measured plume widths.

The results may be summarized as

$$0 \le D_v \le 0.6 \text{ m}^2 \text{ s}^{-1}, \qquad 5 \le D_h \le 20 \text{ m}^2 \text{ s}^{-1}, \quad (39)$$

$$0 \le |D_s| \le 2 \text{ m}^2 \text{ s}^{-1}, \quad (40)$$

with $D_s = 0$ for $D_v = 0$. In section 6 it will be shown that D_v and D_s are probably close to the lower limits.

6. Analysis of Atmospheric Turbulence

In this section we relate the plume properties to the turbulence data. The Falcon aircraft has been used for turbulence research for over a decade. Equipment and accuracy of the measurement system are described, e.g., by *Bögel and Baumann* [1991] and *Hauf* [1993]. Wind components are measured using a five-hole pressure probe at the tip of a nose boom and an inertial navigation system. Mean winds have an accuracy of 1.5 m s^{-1} for the horizontal and 0.3 m s^{-1} for the vertical components. Temperature is measured with Rosemount Pt100

Table 6. Variance (in 10^{-2} m^2 s^{-2}) of Wind Velocities u (East-West), v (North-South), and w (Vertical) Averaged Over One and Ten 1-min Time Intervals Around Peaks

Number	$\langle u'^2\rangle$, 1 min	$\langle u'^2\rangle$, 10 min	$\langle v'^2\rangle$, 1 min	$\langle v'^2\rangle$, 10 min	$\langle w'^2\rangle$, 1 min	$\langle w'^2\rangle$ 10 min
1	6.3	7.7	1.6	8.0	1.4	1.1
2	10.5	9.9	1.6	8.0	1.0	1.1
3	13.2	9.9	7.9	11.8	1.2	1.1
4	8.9	6.8	20.2	11.7	0.96	1.0
5	9.3	11.1	4.5	14.5	0.51	0.94
6	3.4	8.7	4.4	8.9	0.69	1.1
7	2.8	9.1	5.7	15.7	1.1	1.2
8	10.2	27.2	5.9	18.6	0.6	0.84
9	2.5	9.1	10.1	15.7	1.2	1.25
10	9.8	5.3	7.7	10.6	2.6	3.2
	7 ± 3	10 ± 3	7 ± 3	12 ± 3	1.1 ± 0.4	1.2 ± 0.4

In the last row, the mean values of the columns are listed.

and Pt500 sensors with an accuracy of about 0.5 K for the mean values. Turbulence data are recorded with 100 Hz. At 11 km altitude and a speed of $v_F = 185$ m s^{-1}, the instruments and the digitalization system resolve velocity fluctuations in flight direction up to 0.03 m s^{-1}, velocity fluctuations perpendicular to that up to 0.01 m s^{-1}, absolute temperature fluctuations up to 0.01 K, and potential temperature fluctuations up to 0.03 K. The nose boom of the Falcon has a beam frequency of about 18 Hz affecting the velocity measurements perpendicular to the flight direction.

To compare the intensities of turbulence inside and outside the plumes, we consider the mean variances of the east-west, north-south, and vertical wind components $\langle u'^2\rangle$, $\langle v'^2\rangle$, and $\langle w'^2\rangle$, respectively, as determined from 1-min time intervals (11-km flight legs) containing the peak concentrations. These intervals are a little larger than the plume scales. The velocity fluctuations u', v', and w' are the deviations from the corresponding 1-min mean values. Mean variances increase with the length of the time interval for which they are defined, and the vertical velocity variances over the whole flight legs are about 2 to 3 times larger than the velocity variances for 1-min averages. The nose boom oscillations affect these data very little. Table 6 compares the 1-min mean values with "10-min" mean values obtained by averaging the variances over ten "1-min" mean values in consecutive time intervals enclosing the plume events. The results exhibit no significant differences between 1-min and 10-min averages, indicating negligible turbulence contributions from the aircraft wake or from contrail processes at the time of plume encounters, consistent with the crew's observations.

Table 6 shows strong anisotropy of air motions with the horizontal variance being about 10 times larger than the vertical variance. If vertical and horizontal motions would have the same turbulent timescales and if the vertical heat flux is small, then this ratio determines D_h/D_v [*Kaltenbach et al.*, 1994]. However, the horizontal motions have usually larger timescales than the vertical ones [*Lilly*, 1983], so that larger values of D_h/D_v are to be expected. In fact, the results of the previous section suggest D_h/D_v to be larger than 10.

We have to ask, however, whether the flow is actively turbulent or in a collapsed state of wavy motions with little cascading energy toward smaller scales. Active turbulence exists if the Ozmidov scale $L_O = (\varepsilon/N^3)^{1/2}$ is at least 10 times larger than the Kolmogorov scale $\eta = (\nu^3/\varepsilon)^{1/4}$ [*Stillinger et al.*, 1983; *Gerz and Schumann*, 1991]. For smaller L_O/η, turbulence collapses and turbulent mixing ceases. These scales are functions of the dissipation rate ε, the Brunt-Väisälä frequency N, and the molecular viscosity ν of air. Moreover, as a prerequisite for an inertial subrange, the spectra should follow a $-5/3$ power law and represent locally isotropic turbulence.

To check for these conditions, we compute the spectral density functions S_w and S_u (in square meters per second) of vertical and horizontal velocity fluctuations (perpendicular to the flight direction) as a function of frequency f (in hertz), where the integral over Sdf corresponds to the mean variance of the respective fluctuations. The spectra are computed from about 10-min time intervals enclosing the plume peaks. Spectra at other times show similar results.

Figure 11 shows the ratio between S_u and S_w versus f for the various plume segments. This ratio should be one for isotropic turbulence. We see that the ratio is larger than one at low frequencies, consistent with the variance ratio calculated in Table 6, but decreases and approaches 1 near 10 Hz. The result does not exclude the existence of a locally isotropic turbulence range near 10 Hz and above, but for $f < 10$ Hz, the spectrum S_u decays significantly stronger than S_w with f and does not support an inertial range assumption. Figure 12 depicts the measured spectra $M(f) = fS_w(f)$. Here the impact of nose boom oscillations is obvious but limited to a very narrow spec-

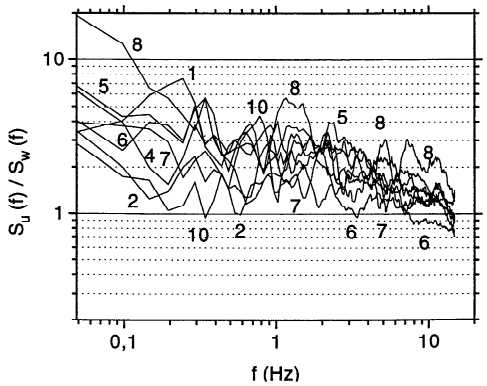

Figure 11. Ratio S_u/S_w of spectral density functions of horizontal and vertical velocity fluctuations versus frequency f for 491-s-long flight segments containing the peaks. The ratio results have been smoothed by averaging over filter bands of 20% relative width. The numbers refer to the peaks within the respective flight segments.

tral range near 18 Hz. At frequencies higher than 1 Hz, $M(f)$ decays approximately as a power law of $M \sim f^n$ with exponents n between -0.7 and -1, not significantly different from the inertial range slope $-2/3$. Only for case 10, the spectrum decays considerably stronger (exponent close to -1.3) but with a trend toward $-2/3$ near 10 Hz.

Hence for an estimate of dissipation rates, we may tentatively assume that the flow is turbulent and possesses an inertial subrange. Since the spectra decay slightly stronger than with $-2/3$, the actual inertial range may follow at the lowest end of the measured range. Therefore dissipation rates deduced from these spectra represent upper bounds for the actual values. In the hypothetical inertial subrange the eddy dissipation rate ε (in $m^2 s^{-3}$) is computed from

$$\varepsilon = \frac{2\pi f}{v_F}\left(\frac{M(f)}{c_k}\right)^{3/2}, \qquad (41)$$

where $c_k = 0.66$ is the Kolmogorov constant for one-dimensional spectra of this velocity component [*Saddoughi and Veeravalli*, 1994], and v_F is the speed of the Falcon. For $M \sim f^{-2/3}$ in the inertial range, ε should be independent of f. A fit of this relation to the measured spectra near 10 Hz results in the values listed in Table 7. The fluctuations of the spectra relative to the fitted mean inertial-range spectra suggest uncertainties in ε of about 30%. The results show that the plume motions experience turbulent dissipation rates which are at least 100 times smaller than the value 10^{-5} $m^2 s^{-3}$ expected climatologically [*Tank*, 1994]. The dissipation results imply very small Ozmidov scales between 0.04 and 0.15 m, only a little larger than the Kolmogorov scales of between 0.02 and 0.05 m (for $\nu \approx 4 \times 10^{-5}$ $m^2 s^{-1}$ [*Pruppacher and Klett*, 1978]). Resolution of motions at these scales would require Falcon measurement frequencies v_F/L_O above 1000 Hz. Thus all the measured motions are, in fact, heavily impacted by buoyancy, and the flow is to be considered as collapsed turbulence. An inertial subrange does not exist for these cases and the turbulent dissipation rate is essentially zero.

Table 7. Turbulence Properties

Number	ε, 10^{-8} $m^2 s^{-3}$	L_O, m	L_K, m	$D_v(\varepsilon)$, 10^{-5} $m^2 s^{-1}$	$D_v(w'^2)$, $m^2 s^{-1}$
1	7.9 ± 0.7	0.12	0.02	2.5	0.08
2	5.7 ± 1.4	0.10	0.03	1.8	0.06
3	5.7 ± 1.4	0.10	0.03	1.8	0.07
4	10 ± 2.0	0.12	0.03	3.2	0.05
5	16 ± 3.0	0.15	0.02	5.0	0.03
6	1.4 ± 0.5	0.06	0.04	0.6	0.05
7	1.7 ± 0.5	0.06	0.04	0.7	0.07
8	10 ± 2.0	0.14	0.03	2.8	0.03
9	10 ± 2.0	0.14	0.03	4.4	0.08
10	1.1 ± 0.2	0.04	0.05	0.4	0.16

Here ε, upper bound for dissipation rate of turbulent kinetic energy; L_O, Ozmidov scalc; L_K, Kolmogorov scalc; $D_v(\varepsilon)$ and $D_v(w'^2)$, upper bound vertical turbulent diffusivities for given ε and for 1-min mean value of the vertical velocity variance $\langle w'^2 \rangle$, respectively.

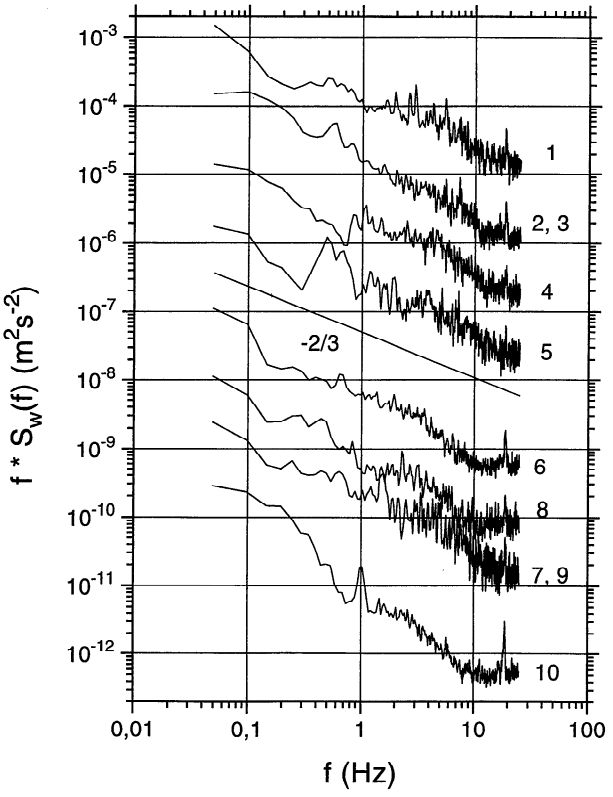

Figure 12. Spectral density function $M(f) = fS_w(f)$ (nonfiltered) of vertical velocity fluctuations versus frequency f. The numbers refer to the peaks within the respective flight segments as in Figure 11. To separate the curves, $M(f)$ has been reduced before plotting by a factor 1 (for 1), 10 (for 2, 3), 100 (for 4), etc.

Some theories relate the vertical eddy diffusivities of heat or passive scalars to either the dissipation rate or the vertical velocity variance and the Brunt-Väisälä frequency N,

$$D_v(\varepsilon) = c_h \frac{\varepsilon}{N^2}, \qquad (42)$$

$$D_v(w'^2) = c_N \frac{w'^2}{N}. \qquad (43)$$

Earlier investigators assumed constant coefficients c_h and c_N, independent of Ri; for example, $c_h = 1/3$ and 0.2 according to *Lilly et al.* [1974] and *Weinstock* [1992], and $c_N = 0.17$ according to *Hunt et al.* [1985]. *Schumann and Gerz* [1995] analyzed mixing in homogeneous turbulence under uniform shear and stratification for $Ri < 1$. They show that the above relations apply with coefficients c_h and c_N which are both close to 0.16 for $Ri = 0.2$. For $Ri = 1$, the coefficients are smaller (0.01 and 0.02, respectively), and they become practically zero for larger Ri. Hence these models give upper bounds for the turbulent diffusivities for $Ri > 1$ when applied with $c_h = c_N = 0.1$. These bounds are listed in Table 7. We find that the models predict small values, as to be expected for large Richardson numbers with collapsed turbulence. The molecular diffusivity of NO in 10 km altitude amounts to 5×10^{-5} $m^2 s^{-1}$ [*Ghosh*, 1993]. This value is greater than the dissipation-based upper estimates. Hence the vertical mixing by (ordinary) turbulence is negligibly small in this situation.

The model predictions are consistent with explanations given by *Hunt* [1985]. For a roughly equal partition between kinetic and potential energy of turbulent motions in a stratified flow (without external energy sources), the fluid elements can only be displaced through a vertical distance of the order of w'/N. The related motion timescales are of the order of $2\pi/N$, i.e., of about 5 min for $N \approx 0.02$ s^{-1}. In our cases the

Table 8. Variance Under Spectrum at 12.5- to 25-km Wavelength for Various Flight Legs

Date	FL, hft	S/T	$\langle u'^2 \rangle$, $m^2\ s^{-2}$	$\langle v'^2 \rangle$, $m^2\ s^{-2}$	$\langle \theta'^2 \rangle$, K^2
October 16	310	T	0.025	0.028	0.009
October 16	350	T	0.051	0.041	0.010
October 17	330	T	0.032	0.045	0.004
October 17	370	T, S	0.055	0.067	0.020
October 20	370	S	0.083	0.067	0.038
		T	0.100	0.110	0.042
		S	0.147	0.168	0.116

In the last two rows, the mean values over ocean from *Nastrom and Gage* [1985] are listed. S/T denotes stratospheric/tropospheric conditions, respectively.

root-mean-square vertical velocity fluctuations w' are less than 0.3 m s^{-1}, even including slow wavy fluctuations along the total flight legs. Hence the vertical motions cause a displacement of less than 15 m and the relatively quick vertical mixing by these motions vanishes when the plumes have spread over this range. Ongoing vertical dispersion at later times requires small-scale mixing, converting part of the kinetic energy into potential energy, at a rate related to dissipation ε. Since the dissipation rate is small or zero in our cases, this late-period mixing has to be weak. In fact, the σ_v data are consistent with zero growth rates at late times (see Figure 8). Hence, vertical plume mixing in our cases is not controlled by turbulence of the ambient atmosphere but mainly caused by the mixing in the vortex regime. Mixing at synoptic scales will become important at much later times.

The horizontal diffusivity can be estimated according to Prandtl's classical concept from the product of horizontal velocity fluctuations and the plume scale. For a widening plume, the relevant velocity fluctuations grow. Hence D_h should be time dependent in principle. For typical values, $\sigma_h = 500$ m, and $u' = 0.3$ m s^{-1}, we obtain $D_h = c_h \sigma_h u' = 15$ $m^2\ s^{-1}$, for $c_h = 0.1$. *Kaltenbach et al.* [1994] found that c_h, based on integral scales of turbulence, is about 0.8 for $Ri = 0$, 0.4 for $Ri = 1$, and decreases with growing Ri. Hence a value $c_h = 0.1$ appears to be reasonable for strongly stratified situations.

The question of how typical the situation is under which the present measurements took place in comparison to turbulence climatologies remains to be discussed. *Lilly et al.* [1974] report statistics of vertical velocity fluctuations from 285 measurement flights with aircraft between altitudes of 14 and 21 km. Only 2% of all flight legs over oceans showed perceptible turbulence with vertical velocity fluctuations exceeding 0.15 m s^{-1} at wavelengths larger than 610 m, which is comparable with our measured w' values. However, our flights took place at lower altitudes. For altitudes of subsonic air traffic, *Nastrom and Gage* [1985] report turbulence statistics from 6000 commercial airliner flights, for which horizontal winds were determined from the routine inertial navigation systems and conventional pressure sensors. From the measured spectra of horizontal velocity fluctuations and of temperature fluctuations, they deduce the variances in the wavelength ranges from 12.5 to 25 km and from 150 to 450 km. The latter is too large for reliable statistics from our data. However, we have evaluated comparable statistics in the range 12.5–25 km from spectra for each of the five flight legs averaging over six to nine segments of 512 s each with 10-Hz resolution (see Table 8). We find that the variances in our cases are about 2 to 4 times smaller than those found on average over the oceans. Further analysis of the commercial aircraft data by *Fritts and Nastrom* [1992] suggests that our results may be representative for cases over oceans away from strong sources of mesoscale variability (such as jet streams, convection, and fronts), but this needs to be investigated further.

7. Conclusions

The dispersion of chemically passive species from a line source in a stably stratified and sheared atmosphere with anisotropic turbulent diffusivities has been described in terms of a Gaussian plume model with an explicit analytical solution. A theoretical framework has been given for the determination of the horizontal and vertical diffusivity coefficients from the concentration profiles observed by in situ measurements of aircraft plumes in the dispersion and diffusion regimes and from estimates of the plume sources. In addition, turbulence data are used to estimate the magnitude of the effective diffusivities.

From measurements of NO obtained in 10 plumes of airliners at cruising altitude near the tropopause over the North Atlantic, these relations are applied to determine the apparent lateral plume width. The Gaussian model is used first to determine the vertical and horizontal scales and the tilting of the plume by shear. Second, it is used for analysis of the eddy diffusivities. The model is supposed to be appropriate for the first purpose. The assumption of constant diffusivities and constant shear is only made to obtain estimates of the effective mean diffusivities from the available data. In reality, the horizontal diffusivities grow with the plume scale and the related horizontal velocity fluctuations. In contrast to previous approaches [*Knollenberg*, 1972; *Joseph et al.*, 1975] we were able to separate the effects from vertical and horizontal turbulent diffusion and from wind shear. The present method provides a direct measure of vertical plume scales, and the plume should be better represented by nitrogen oxides data than by the nonconservative contrail properties. The plume analysis results in preliminary values D_v between 0 and 0.6 $m^2\ s^{-1}$, D_h between 5 and 20 $m^2\ s^{-1}$, and D_s between 0 and about 2 $m^2\ s^{-1}$. These results are consistent in magnitude with previous estimates [*Lilly et al.*, 1974; *Knollenberg*, 1972; *Joseph et al.*, 1975].

Simultaneous turbulence data show no residuals of aircraft or contrail-induced turbulence at the time of plume encounters, i.e., for plumes older than 5 min. The vertical velocity variance at plume scales is 10 times smaller than the horizontal ones. It is too small to explain the observed plume dispersion. The spectral analysis shows that all scales up to the viscous scales are affected by buoyancy causing practically zero turbulent dissipation and vanishing vertical turbulent mixing, so that $D_v \approx 0$, $D_s \approx 0$ due to turbulence in the dispersion range. This finding is consistent with the range of values deduced from the plume analysis. The initial impulse of aircraft lift causes sufficient vertical motions to explain the observed vertical dispersion. Hence for plumes of ages between several minutes and a few hours and for cases with strong stable stratification, we recommend $D_v = 0$, D_h between 5 and 20 $m^2\ s^{-1}$, and $D_s = 0$.

Obviously, the small number of the measured NO peaks does not represent a large statistical ensemble. Hence this paper basically shows that horizontal and vertical diffusivities can be estimated from plume data by the given methods, while the resultant values should still be taken with care. In the

future we intend to apply the same tools to further plume observations, including multiple measurements in the same plume at various ages.

The Gaussian model shows that the lateral plume width grows with $(2s^2D_v t^3/3)^{1/2}$ for finite vertical diffusivity, and with $s\sigma_{0v}t$ for zero vertical diffusivity in the final period, and not with $(2D_h t)^{1/2}$ as in cases without shear. Hence any "effective horizontal diffusivity" will depend on time because of the growing scale range of horizontal turbulence at early times and because of dominating shear at late times. For typical values of this study, $s \approx 0.002\ s^{-1}$, $D_v \approx 0$, $D_h \approx 15\ m^2\ s^{-1}$, and $\sigma_{0v} \approx 50$ m; shear dominates the lateral dispersion after the time $2D_h/(\sigma_{0v}s)^2$ of about 1 hour.

The results of this study represent flight route conditions with strongly, stably stratified and weakly sheared atmospheric situations. The comparison to statistics of *Nastrom and Gage* [1985] suggests that we were measuring in a situation with less than average turbulence. The frequency of and the mixing properties in more strongly turbulent cases remain to be determined.

Acknowledgments. We are very grateful to F. Deidewig (DLR, Institute of Propulsion Technology, Cologne) for computing the fuel flow and emission index values, R. Gardner (Department of Transport, London), his consultant, and F. Walle (Lufthansa, Hamburg) for providing information on the aircraft/engine combinations; E. Hare (Atmospheric Environment Service, Downsview, Ontario), J. Ovarlez (Laboratoire Meteorologique Dynamique du CNRS, Palaiseau), and P. van Velthoven (KNMI, Royal Netherlands Meteorological Institute, De Bilt) for help in accessing ozone data; P. Hughes (UK Meteorological Office, Bracknell) for providing the ozonesonde data of the Lerwick Station, to the Civil Aviation Authority (London) for providing access to the flight control data; D. Pake and M. Anteers (ATC, Prestwick) for expert support during the measuring period at Prestwick; and to the Falcon team (DLR, Oberpfaffenhofen) for excellent professional performance in the experimental campaign. The measurements and evaluations were supported by BMFT (German Federal Ministry of Research and Technology) within the DLR-BMFT project "Schadstoffe in der Luftfahrt," and by the Commission of the European Union within the POLINAT research project.

References

Arnold, F., J. Scheid, T. Stilp, H. Schlager, and M. E. Reinhardt, Measurements of jet aircraft emissions at cruise altitude, I, The odd-nitrogen gases NO, NO_2, HNO_2 and HNO_3, *Geophys. Res. Lett.*, *19*, 2421–2424, 1992.

Barat, J., Some characteristics of clear-air turbulence in the middle stratosphere, *J. Atmos. Sci.*, *39*, 2553–2564, 1982.

Bögel, W., and R. Baumann, Test and calibration of the DLR Falcon wind measuring system by maneuvers, *J. Atmos. Oceanic Technol.*, *8*, 5–18, 1991.

Brühl, C., and P. J. Crutzen, Scenarios of possible changes in atmospheric temperatures and ozone concentrations due to man's activities, estimated with a one-dimensional coupled photochemical climate model, *Clim. Dyn.*, *2*, 173, 1988.

Cadet, D., Energy dissipation within intermittent clear air turbulence patches, *J. Atmos. Sci.*, *34*, 137–142, 1977.

Dalaudier, F., C. Sidi, M. Crochet, and J. Vernin, Direct evidence of "sheets" in the atmospheric temperature field, *J. Atmos. Sci.*, *51*, 237–248, 1994.

Danilin, M. Y., B. C. Krüger, and A. Ebel, Short-term atmospheric effects of high-altitude emissions, *Ann. Geophys.*, *10*, 904–911, 1992.

Deidewig, F., Schadstoffemissionen ziviler Flugtriebwerke, *DGLR-Rep. 92-03-084*, Dtsch. Ges. für Luft- und Raumfahrt, Bonn, 1992.

Deidewig, F., and M. Lecht, NO_x emissions from aircraft/engine combinations in flight, in *Impact of Emissions From Aircraft and Spacecraft Upon the Atmosphere*, edited by Schumann, U. and D. Wurzel, *DLR-Mitt. 94-06*, pp. 44–49, Dtsch. Forschungsanst. für Luft und Raumfahrt, Cologne, 1994.

Dewan, E. M., On the nature of atmospheric waves and turbulence, *Radio Sci.*, *20*, 1301–1307, 1985.

Donaldson, C. P., and A. J. Bilanin, Vortex wakes of conventional aircraft, *AGARD-AG-204*, Advis. Group for Aerosp. Res. and Dev., NATO, Brussels, 1975.

Drummond, J. W., A. Volz, and D. H. Ehhalt, An optimized chemiluminescence detector for tropospheric NO measurements, *J. Atmos. Chem.*, *2*, 287–306, 1985.

Fahey, D. W., et al., In situ observations in aircraft exhaust plumes in the lower stratosphere at midlatitudes, *J. Geophys. Res.*, *100*, 3065–3074, 1995.

Fritts, D. C., and G. D. Nastrom, Sources of mesoscale variability of gravity waves, II, Frontal, convective, and jet stream excitation, *J. Atmos. Sci.*, *49*, 111–127, 1992.

Gelinas, R. J., and J. J. Walton, Dynamic-kinetic evolution of a single plume of interacting species, *J. Atmos. Sci.*, *31*, 1807–1813, 1974.

Gerz, T., and U. Schumann, Direct simulation of homogeneous turbulence and gravity waves in sheared and unsheared stratified flows, in *Turbulent Shear Flows*, edited by F. Durst et al., pp. 27–45, Springer-Verlag, New York, 1991.

Ghosh, S., On the diffusivity of trace gases under stratospheric conditions, *J. Atmos. Chem.*, *17*, 391–397, 1993.

Hagen, D. E., P. D. Whitefield, and M. B. Trueblood, Particulate characterization in the near field of commercial transport aircraft exhaust plumes using the UMR-MASS, in *Impact of Emissions From Aircraft and Spacecraft Upon the Atmosphere*, edited by Schumann, U. and D. Wurzel, *DLR-Mitt. 94-06*, pp. 119–124, Cologne, 1994.

Hauf, T., Aircraft observation of convection waves over Southern Germany—A case study, *Mon. Weather Rev.*, *121*, 3282–3290, 1993.

Hoinka, K. P., M. E. Reinhardt, and W. Metz, North Atlantic air traffic within the lower stratosphere: Cruising times and corresponding emissions, *J. Geophys. Res.*, *98*, 23,113–23,131, 1993.

Hoshizaki, H., L. B. Anderson, R. J. Conti, N. Farlow, J. W. Meyer, T. Overcamp, K. O. Redler, and V. Watson, Aircraft wake microscale phenomena, in *The Stratosphere Perturbed by Propulsion Effluents*, chap. 2, *CIAP, DOT-TST-75-53*, Natl. Tech. Inf. Serv., Springfield, Va., 1975.

Hunt, J. C. R., Diffusion in the stably stratified atmospheric boundary layer, *J. Clim. Appl. Meteorol.*, *24*, 1187–1195, 1985.

Hunt, J. C. R., J. C. Kaimal, and J. E. Gaynor, Some observations of turbulence structure in stable layers, *Q. J. R. Meteorol. Soc.*, *111*, 793–815, 1985.

Jane, *Jane's All the World's Aircraft 1975–76*, edited by J. W. R. Taylor, Jane's Yearbooks, London, 1976.

Joseph, J. H., Z. Levin, Y. Mekler, G. Ohring, and J. Otterman, Study of contrails observed from ERTS 1 satellite imagery, *J. Geophys. Res.*, *80*, 366–372, 1975.

Kaltenbach, H.-J., T. Gerz, and U. Schumann, Large-eddy simulation of homogeneous turbulence and diffusion in stably stratified shear flow, *J. Fluid Mech.*, *280*, 1–40, 1994.

Karol, I. L., and Y. E. Ozolin, Small- and medium-scale effects of high-flying aircraft exhausts on the atmospheric composition, *Ann. Geophys.*, *12*, 979–985, 1994.

Knollenberg, R. G., Measurements of the growth of the ice budget in a persisting contrail, *J. Atmos. Sci.*, *29*, 1367–1374, 1972.

Konopka, P., Analytical Gaussian solutions for anisotropic diffusion in a linear shear flow, *J. Non-Equilib. Thermodyn.*, *20*, 78–91, 1995.

Lilly, D. K., Stratified turbulence and the mesoscale variability of the atmosphere, *J. Atmos. Sci.*, *40*, 749–761, 1983.

Lilly, D. K., D. E. Waco, and S. I. Adelfang, Stratospheric mixing estimated from high-altitude turbulence measurements, *J. Appl. Meteorol.*, *13*, 488–493, 1974.

Miake-Lye, R. C., M. Martinez-Sanchez, R. C. Brown, and C. E. Kolb, Plume and wake dynamics, mixing, and chemistry behind a high speed civil transport aircraft, *J. Aircraft*, *30*, 467–479, 1993.

Monin, A. S., and A. M. Yaglom, *Statistical Fluid Mechanics: Mechanics of Turbulence*, vol. 1, MIT Press, Cambridge, Mass., 1971.

Nastrom, G. D., and K. S. Gage, A climatology of atmospheric wavenumber spectra of wind and temperature observed by commercial aircraft, *J. Atmos. Sci.*, *42*, 950–960, 1985.

Novikov, Y. A., Turbulent diffusion in a shear flow, *Prikl. Matem. Mekh.*, *22*, 412, 1958.

Pruppacher, H. R., and J. D. Klett, *Microphysics of Clouds and Precipitation*, D. Reidel, Norwell, Mass., 1978.

Rodriguez, J. M., R.-L. Shia, M. K. W. Ko, C. W. Heisey, D. K. Weisenstein, R. C. Miake-Lye, and C. E. Kolb, Subsidence of air-

craft engine exhaust in the stratosphere: Implications for calculated ozone depletions, *Geophys. Res. Lett.*, *21*, 69–72, 1994.

Ruggaber, A., R. Dlugi, and T. Nakajima, Modelling of radiation quantities and photolysis frequencies in the troposphere, *J. Atmos. Chem.*, *18*, 171–210, 1994.

Saddoughi, S. G., and S. V. Veeravalli, Local isotropy in turbulent boundary layers at high Reynolds numbers, *J. Fluid Mech.*, *268*, 333–372, 1994.

Schlager, H., P. Schulte, H. Volkert, R. Busen, and U. Schumann, Observations of enhanced nitric oxide abundances within the North Atlantic flight corridor, in *Impact of Emissions From Aircraft and Spacecraft Upon the Atmosphere*, edited by Schumann, U. and D. Wurzel, *DLR-Mitt. 94-06*, pp. 336–341, Cologne, 1994.

Schumann, U., On the effect of emissions from aircraft engines on the state of the atmosphere, *Ann. Geophys.*, *12*, 365–384, 1994.

Schumann, U., and T. Gerz, Turbulent mixing in stably stratified shear flows, *J. Appl. Meteorol.*, *34*, 33–48, 1995.

Schumann, U., and P. Konopka, A simple estimate of the concentration field in a flight corridor, in *Impact of Emissions From Aircraft and Spacecraft Upon the Atmosphere*, edited by Schumann, U. and D. Wurzel, *DLR-Mitt. 94-06*, pp. 354–359, Cologne, 1994.

Smith, R., Dispersion of tracers in the deep ocean, *J. Fluid Mech.*, *123*, 131–142, 1982.

Stillinger, D. C., K. N. Helland, and C. W. van Atta, Experiments on the transition of homogeneous turbulence to internal waves in a stratified fluid, *J. Fluid Mech.*, *131*, 91–122, 1983.

Tank, W., A climatology of lower stratosphere clear air turbulence, in *32nd Meeting on Aerospace Sciences, AIAA 94-0377*, 18 pp., Am. Inst. of Aeronaut. and Astronaut., New York, 1994.

Weinstock, J., Vertical diffusivity and overturning length in stably stratified turbulence, *J. Geophys. Res.*, *97*, 12,653–12,658, 1992.

Woodman, R. F., and P. K. Rastogi, Evaluation of effective eddy diffusivity coefficients using radar observations of turbulence in the stratosphere, *Geophys. Res. Lett.*, *11*, 243–246, 1984.

Young, W. R., P. B. Rhines, and C. J. R. Garrat, Shear-flow dispersion, internal waves and horizontal mixing in the ocean, *J. Phys. Oceanogr.*, *12*, 515–527, 1982.

R. Baumann, R. Busen, T. Gerz, P. Konopka, H. Schlager, P. Schulte, U. Schumann (corresponding author), and H. Volkert, DLR, Institut für Physik der Atmosphäre, Oberpfaffenhofen, Postfach 1116, 82230 Wessling, Germany.

(Received December 7, 1994; accepted March 31, 1995.)